Viscous Effects and Truncation Effects in Axisymmetric Busemann SCRamjet Intakes

Andreas K. Flock*, Ali Gülhan†
German Aerospace Center (DLR), 51147 Cologne, Germany

While designing a Busemann intake, we encountered two main constraints: First, caused by the displacement of the boundary layer, the pressure levels in a Busemann intake were higher ($\approx 40\%$) than the values predicted analytically; these effects were labeled viscous effects. Second, truncating the flow field also changed the properties of the classical Busemann flow; these effects were labeled truncation effects and we distinguished between truncating the intake at the leading edge and at the rear side. To take into account viscous effects, we calculated the boundary layer displacement thickness with an integral method and widened the inviscid Busemann contour. To quantify the leading edge truncation effect, an oblique shock at the leading edge was assumed, and also the intake contraction ratio was stretched. The change in flow properties during the rear side truncation was derived in a stream thrust analysis. We separately investigated the effects with Reynolds-averaged Navier-Stokes and Euler simulations, respectively. After the viscous correction, the deviation between numerically and analytically calculated pressure levels was below 10%. When truncating at the leading edge, the numerically calculated pressure level was generally too low, while the temperature level was within 5% of the prediction. After stretching the contraction ratio, we were able to keep the pressure within 5% of the design value, however in this case, the temperatures were generally too high. The stream thrust approach was highly accurate and for rear side truncated intakes we were able to predict the numerical pressure and temperature levels within 1% of the design values.

Nomenclature

A	cross sectional area, $[\mathrm{m}^2]$	str-thr-av	stream thrust averaged
CR	contraction ratio	T	temperature, [K]
CV	control volume	tp	transition parameter
c_p	heat capacity at const. pressure, $[\mathrm{J/kg/K}]$	v	normalized, regular velocity, $[-,\mathrm{m/s}]$
$\vec{F}$	force vector, [N]	w/woVC	with/without viscous correction
h	altitude, [m]; height, [m];	x, y, z	local coordinates, [m]
	specific enthalpy, $[\mathrm{J/kg}]$	α	flow angle, $[^\circ]$
L	length, [m]	γ	ratio of specific heats for air
LE	leading edge	δ	truncation angle, $[^\circ]$
M	Mach number	δ_1	displacement thickness, [m]
$\dot{m}$	mass flow, $[\mathrm{kg/s}]$	δ_2	momentum thickness, [m]
mav	mass averaged	Θ	temperature ratio
$\vec{n}$	normal vector	θ	fan angle
p	pressure, $[\mathrm{N/m}^2]$	Π	pressure ratio
Re	Reynolds number, $\rho v x/\mu$	ρ	density, $[\mathrm{kg/m}^3]$
r	radius, [m]		

Subscript

3	isolator location	o	overall portion
cc	combustion chamber position	r	radial direction
cl	cowl closure position	st	static condition
e	edge location	tot	total condition
i	arbitrary index	w	wall
i	internal portion	θ	circumferential direction
inv	inviscid	∞	free stream condition

*PhD Candidate, Supersonic and Hypersonic Technology Department, Institute of Aerodynamics and Flow Technology, Linder Höhe, 51147 Cologne, Germany, Student Member

†Department Head, Supersonic and Hypersonic Technology Department, Institute of Aerodynamics and Flow Technology, Linder Höhe, 51147 Cologne, Germany

I. Introduction

When supersonic flight speeds are exceeded and the hypersonic flight regime is approached, conventional turbojet engines lose their practicality and Ram powered engines, such as Ram- or Supersonic Combustion (SC) Ramjet engines become advantageous[1]. While in turbojet engines, the air intake is followed by a compressor, in a SCRamjet engine there are no compressor stages, but rather all compression is achieved by the ram compression within the air intake. Therefore the design of the air intake becomes crucial for a successful operation of the entire engine[2].

The current work was performed within a subproject of the Research Training Group 1095[3], which investigates aero-thermal effects, that occur within a SCRamjet engine. More specifically, the subproject is focused on the design of hypersonic air intakes, with the goal to define a fully tree-dimensional air intake geometry. During previous studies, two-dimensional ramp intakes were investigated[4,5]. Furthermore, a three-dimensional intake was designed by means of computational fluid dynamics (CFD)[6,7], and experimentally tested in a blow down wind tunnel at $M = 7$ and $M = 6$[8].

In the present paper, we focus on axisymmetric intakes. Van Wie[2] distinguished between the following two kinds: (1) outward turning air intakes, such as the spike diffuser intake[9] or the Oswatitsch[10] intake and (2) inward turning air intakes, such as the Busemann air intake[11] or reversed nozzle geometries, that are designed with the method of characteristics[12–14]. To intakes of the latter kind, a so called streamline tracing procedure can be applied, with which fully three-dimensional air intakes can be designed[15–17].

In the following subsections we are first going to explain the design methodology for a classical Busemann geometry, and we will point out, why it is important to gain a proper understanding of the axisymmetric flow field. After that, we will focus on some practical constrains, which introduce modifications from the classical geometry. These practical constraints are summarized as viscous effects and truncation effects, while in the latter case we distinguished between intakes which were truncated at the leading edge and intakes which are truncated at the rear side. Subsequently, the effects will be analyzed numerically and the numerical procedure along with the reference configuration is explained. In section III., we will point out in what way the viscous effects and truncation effects influence the classical Busemann flow field.

A. The Classical Busemann Intake

The assumptions for a Busemann flow are (i) inviscid, (ii) axisymmetric and (iii) irrotational flow and the flow field is described by the Taylor-McColl equations for conical flow[14,18]:

$$v_{\mathrm{r}}'^2\left(v_{\mathrm{r}}+v_{\mathrm{r}}''\right)=\frac{\gamma-1}{2}\left(1-v_{\mathrm{r}}^2-v_{\mathrm{r}}'^2\right)\left(v_{\mathrm{r}}''+v_{\mathrm{r}}'\cot(\theta)+2v_{\mathrm{r}}\right) \tag{1a}$$

$$v_{\mathrm{r}}'=v_\theta \tag{1b}$$

in which θ, v_{r} and v_θ are the fan angle, radial and tangential velocity, and where γ is the ratio of specific heats for air. A principal sketch of the resulting flow field is displayed as the solid gray line in figure 1. The undisturbed free stream is at first compressed isentropically, and the flow field is characterized by fan like lines along which the flow properties (p, T, M) are constant. The isentropic compression is finalized by a conical shock, after which the air stream is again homogeneous. The velocities v_{r} and v_θ are arranged along the fan like lines and perpendicular to them, respectively, and are normalized to the velocity that would be reached if the fluid was expanded isentropically to $T = 0\mathrm{K}$. The angle, θ_i, is spanned by the fan like lines and the x-direction. The following relationship between normalized velocity, v, and Mach number can be arranged:

$$\sqrt{v_{\mathrm{r}}^2+v_\theta^2}=v=\sqrt{\frac{(\gamma-1)M^2}{2+(\gamma-1)M^2}} \tag{2}$$

The radial velocity, v_{r}, can be calculated as a function of θ, by integrating equation (1a) over the angle, θ, with the Runge-Kutta algorithm[19]. With equation (1b), the tangential velocity coordinate, v_θ, is calculated and finally the Mach number at each position, θ_i, can be determined via equation (2). An iterative procedure has to be implemented, if the design variables are different from the initial variables, M_3 and θ_3. By following the streamline of a single position across the region of the isentropic compression, the Busemann geometry is defined. In the subsequent context, the radius of the Busemann flow field at the intake exit will be defined as the combustion chamber height, h_{cc}, and all other dimensions will be given as fractions of it. Please note, that to this point the Busemann geometry is scale independent and can be stretched to any arbitrary size.

To further emphasize, why it is important to gain a fundamental understanding of the axisymmetric Busemann flow field, in figure 2 two contour plots of the same streamline traced intake are shown. The intake was extracted from a classical axisymmetric Busemann flow, applicable to inviscid flow and without any truncation. On the left hand side, the analytical solution and on the right hand side a numerical Euler solution is displayed. It is highlighted, that the

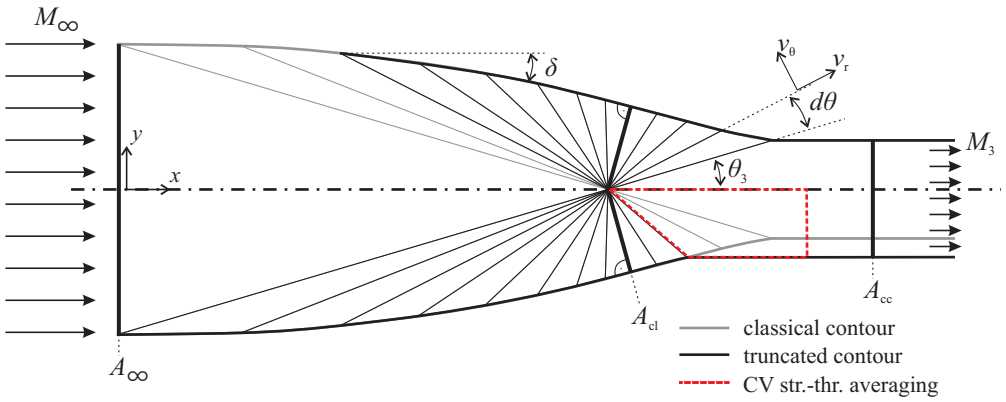

Figure 1. Sketch of a classical Busemann flow field along with leading edge truncated (top) and rear side truncated (bottom) Busemann flow field.

analytical prediction practically does not vary from the inviscid numerical solution. Therefore the axisymmetric flow field forms the very basis of any three-dimensional geometry, which is extracted from it. Furthermore any characteristic measure of the axisymmetric flow field, such as pressure ratio or the degree of non uniformity at the intake exit, will be transformed to the three-dimensional geometry. Therefore it is very important to properly quantify the Busemann flow field, especially when viscous and truncation effects occur. In the following context no further explanation of the streamline tracing approach is presented, but the reader is referred to the literature [15–17].

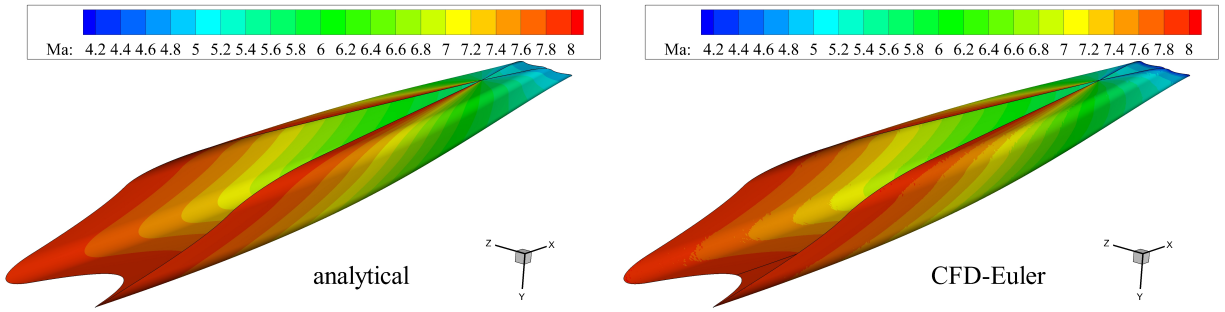

Figure 2. Mach number contour plots of a streamline traced Busemann intake for the analytical solution (left) and Euler simulation (right); geometry designed for $M_\infty = 8, \Pi_{st} = 45$ and $\delta = 0°$

.

B. Viscous Effects

The Taylor-McColl equations, and therefore a Busemann geometry are valid for inviscid flow only. However, viscosity is present in all real flows, and will further contract the flow field. In figure 3, for example, an inviscid, as well as viscous calculation of a classical Busemann geometry are shown and the mass averaged static pressure ratios are displayed. In the Euler simulation, the static pressure ratio deviated only marginally from the design static pressure ratio of 43. However, in the RANS simulation the static pressure ratios exceeded the design static pressure ratio by at least 40%. The pressure ratios were given for two axial positions to highlight the pressure increase in the isolator during the viscous simulation, which was not present in the Euler simulation. Please note, that this effect is scale dependent, and that the displayed RANS simulation was performed for $h_{cc} = 29.4$ mm.

To account for these effects, we adapted the following approach, which can be found in the literature [15,16,20]: The pressure distribution of the inviscid Busemann geometry is taken as the edge pressure of a boundary layer. Assuming constant total conditions at the boundary layer edge, the displacement thickness can be calculated. Finally, the inviscid Busemann geometry is widened normal to its surface by the calculated displacement thickness, and therefore the isentropic compression within the core flow field is maintained. This newly calculated geometry is in the further context referred to as the corrected Busemann geometry.

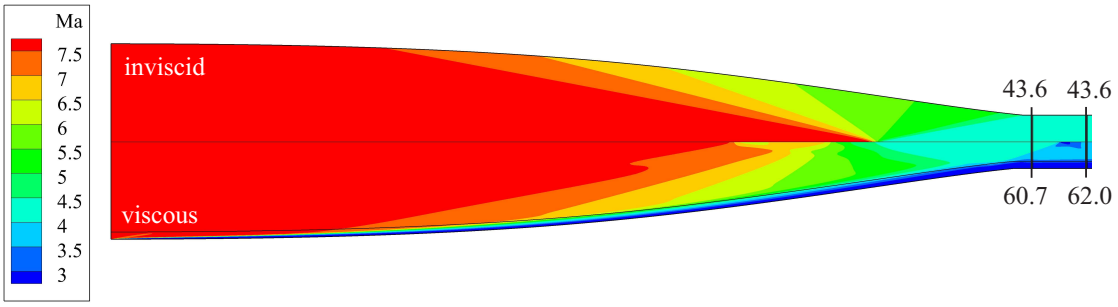

Figure 3. Euler (top) and RANS (bottom) simulations of axisymmetric Busemann geometries without viscous correction; intake was designed for $M_\infty = 8, \Pi_{st} = 43, \delta = 0°$ and $h_{cc} = 29.4$ mm; at exit, mass averaged static pressure ratios at two axial positions are given.

C. Truncation Effects

1. *Leading Edge Truncation*

Another restriction for the classical Busemann flow field, comes with the inflow condition at the leading edge. The gradual deflection from the stream wise direction, which is required for the isentropic compression, is a critical configuration for two reasons: First, the geometry tends to become excessively long, which itself increases friction drag and, in an overall analysis might reduce the benefit of an isentropic compression. Second, there are manufacturing restrictions on how sharp the leading edges or the minimum wall thickness can be.

To overcome the described problems, those kind of intakes usually have to be truncated at the leading edge, which is indicated on the top portion of figure 1 and 4. Truncation angles of approximately $\delta = 2°$ to $5°$ are sufficiently large to manage manufacturing restrictions and to reduce the intake length significantly. The oblique shock, emanating at the leading edge however, distorts the isentropic compression of the classic Busemann flow. Furthermore, the calculated static pressure ratio at the intake exit does not necessarily match the design static pressure ratio.

The truncation effect was also investigated in a numerical study for inviscid flows by Zhao[21], up to truncation angles of $\delta = 6°$. Zhao reported, that with increasing truncation angle an oblique shock emanates from the leading edge and that it distorts the flow field. Furthermore, the intake efficiency decreased with increasing truncation angle. However viscous effects were not considered, and therefore no comment on the trade off between skin friction drag and wave drag was made.

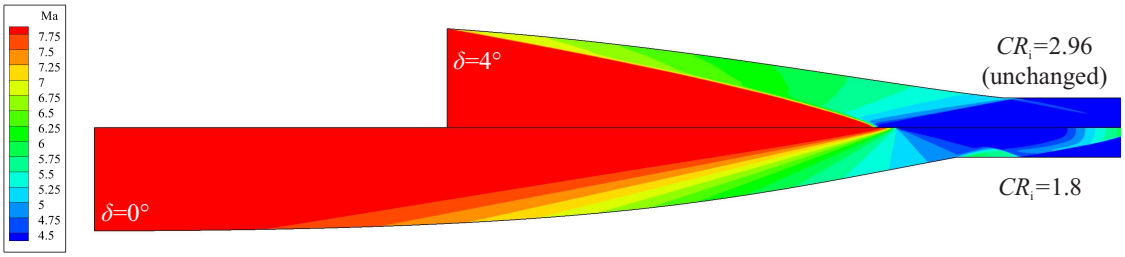

Figure 4. Euler simulations of leading edge truncated (top) and rear side truncated (bottom) axisymmetric Busemann geometries for $M_\infty = 8$ and $\Pi_{st} = 43$.

2. *Rear Side Truncation*

The principle of rear side truncation is displayed in the bottom part of figure 1 and 4. The isentropic compression is not brought to a complete end, but the transition to the isolator is set to a specific location. This generates a non uniform flow at the intake exit, and changes the performance parameters. In section II. we will explain, how the changed parameters can be estimated with a stream thrust averaging approach.

There are three advantages of truncating a classical Busemann intake from the rear side: First, the intake length can be reduced. As mentioned earlier, there is a trade-off between friction drag and an optimum amount of isentropic compression. Because the leading edge truncation induces an oblique shock at the highest Mach number possible, and therefore high shock losses, the leading edge truncation angle should be limited. To further reduce intake length, it can be appropriate to truncate the intake at the rear side.

Second, when a streamline tracing approach is applied to generate a fully three-dimensional SCRamjet intake (figure 2), truncating the intake at the rear side reduces the internal contraction ratio and consequently intake starting

is enhanced. The internal contraction ratio is defined as the ratio of the cross sectional area at the cowl closure position, A_{cl}, over the cross section area at the intake exit, A_{cc}, and is therefore a purely geometrical feature of an intake. A so called strong-shock design principle was proposed by Veillard[22], which is to an extend comparable to the rear side truncation, and with which intake starting could be enhanced. For more detailed information on intake starting please refer to the cited literature[8,23–25].

Third it is noted, that in a classical Busemann intake the flow at the interface to the combustion chamber will be homogeneous. Molder noted, that this is required to maintain a high compression efficiency[18]. Furthermore von Wie pointed out that an intake with non uniform exit profile is less robust concerning intake unstart[2]. However, mixing can be enhanced by non uniform flows. Furthermore, the temperature profile throughout the isolator will be non uniform, while regions with locally increased temperature could improve ignition. Finally it is noted, that the desired state of the flow within the isolator is somewhat dependent on the design philosophy or concept of the individual designer or SCRamjet group.

II. Methods and Materials

In the following subsections we present the approach to the previously described constraints: Viscous effects and truncation effects. Furthermore the reference configuration is described, along with the numerical setup, that builds the frame for the investigations.

A. Approach to Viscous Effects

To avoid the additional contraction of the viscous boundary layer, we used the previously mentioned approach and widened the Busemann intake by the boundary layer displacement thickness. We used an integral method by Walz[26], that is applicable to laminar as well as turbulent flows. We calculated the displacement thickness along the Busemann contour with the given wall pressure, which acted as the boundary layer edge pressure. In the isolator, the height remained constant.

In figure 5, the edge pressure distribution of a Busemann flow field, which was designed for a free stream Mach number of 8, and a static pressure ratio of 43 is displayed. The contour was not truncated and the continuous isentropic compression is clearly visible. Please note, that the pressure jump, due to the final conical shock is not displayed. Furthermore, a fully laminar (lam) as well as fully turbulent (turb) boundary layer displacement thickness are plotted in figure 5, versus the free stream direction. Besides, transition was gradually introduced, depending on $Re_{\delta_2}/M_{\mathrm{e}}$ (trans). The dataset of Berkowitz[27] was used, to define the transition region between

$$56 < Re_{\delta_2}/M_{\mathrm{e}} < 461 \tag{3}$$

and in this range, the displacement thickness was gradually lead from laminar to turbulent. A more detailed explanation of this gradual transition can be found in appendix A.

For the laminar case, the integral method predicted separation at $\approx -0.1\ \mathrm{m}$, and the displacement thickness was forced to zero. However, due to the very high Reynolds number at that position ($Re_{\delta_2}/M_{\mathrm{e}} > 461$), it is unlikely that the flow remains laminar and therefore the laminar separation was irrelevant.

At the leading edge, the fully turbulent boundary layer displacement thickness was smaller than the fully laminar one and exceeded the laminar boundary layer at $x > -0.85\ \mathrm{m}$. We believe the reason for this was, that the boundary layer was forced to be fully turbulent at locations very far upstream. A turbulent boundary layer is fuller and therefore its displacement, relative to its boundary layer thickness, is lower, than in a laminar boundary layer[28]. Therefore the turbulent boundary layer was initially lower, than the laminar one.

The displacement thickness with gradual transition, based on the data set of Berkowitz[27] showed a continuous transfer from laminar to turbulent. It is noted, that the fully turbulent boundary layer thickness and the transitional case matched each other at $x > -0.4\ \mathrm{m}$ only by accident.

We further investigated the corrected Busemann geometries with CFD, and the numerical modeling will be explained in a following subsection. Since we used a turbulent wall condition for the simulations, the boundary layer displacement thickness for a fully turbulent wall was used for widening the Busemann geometry.

B. Approach to Truncation Effects

1. Leading Edge Truncation

The leading edge truncation of the Busemann geometry is necessary, to reduce the intake length and therefore skin friction, and also to avoid the 0° inflow and the problems connected to it. However, the truncation causes an oblique shock at the leading edge which disturbs the isentropic compression flow field. In the present study, we truncated Busemann intakes at the leading edge in steps of 1° and investigated truncation angles up to 7°. The pressure increase

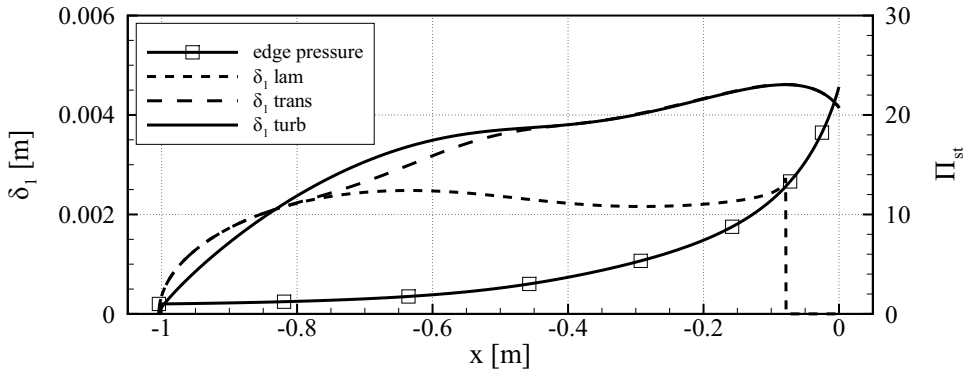

Figure 5. Displacement thicknesses for different boundary layers along with edge pressure distribution plotted versus the free stream direction.

at the leading edge was modeled with a two-dimensional oblique shock, with the free stream Mach number, M_∞, and the deflection angle to be equal to the truncation angle, δ.

In figure 6, the truncated contour is displayed (os - ∇ symbols) for the 4° leading edge truncation as a sample case, along with the reference contour. Furthermore, the truncated geometry was stretched to two larger contraction ratios: First, to the contraction ratio of the reference contour (os stretch - $\triangle$ symbols), and second to the mean contraction ratio between the reference contour and the non modified contour: $0.5\,(CR_{\mathrm{o},\delta=0^\circ} + CR_{\mathrm{o},\delta=i^\circ})$ (os $1/2$ stretch - $\square$ symbols). The reasoning for this step will become clear when the results are discussed in section III. B..

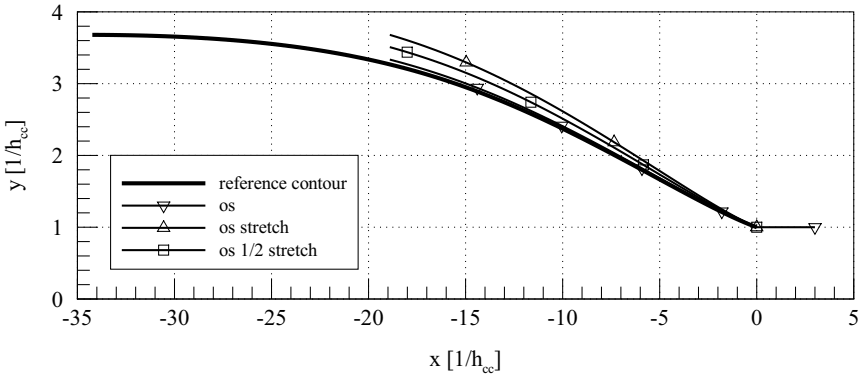

	$L[1/h_{\mathrm{cc}}]$	CR_{o}
ref	34.2	13.54
∇	18.9	11.12
$\triangle$	18.9	13.54
$\square$	18.9	12.32

Figure 6. Classical Busemann geometry, along with different truncated geometries ($\delta = 4^\circ$); furthermore lengths, normalized to isolator height and contraction ratios are given.

2. *Rear Side Truncation*

To calculate the influence of the rear side truncation on the performance parameters, the control volume from figure 1 is enlarged in figure 7. While the symmetry axis and intake wall mark the top and bottom boundary conditions, respectively, the quantities at the entrance, marked by the subscript i were known along with the geometrical features, α_i, θ_i and r_i. With a stream thrust analysis the desired, one-dimensional quantities at the exit, M_3, p_3 and T_3 were calculated as follows:

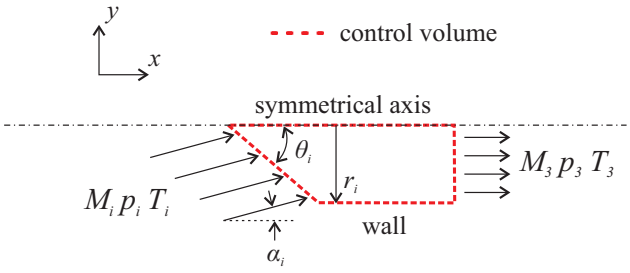

Figure 7. Control volume analysis of truncated portion of Busemann intake.

The mass flow through the control volume was constant, and was calculated via

$$\dot{m}_i = \int (\rho_i \vec{v}_i \cdot \vec{n}_i)\, \mathrm{d}A_i = \rho_3 v_3 A_3 = \dot{m}_3, \tag{4}$$

while the density, ρ, and velocity, v, were calculated from the equation of state for an ideal gas and the definition of Mach number, respectively. Furthermore the total enthalpy was constant, which introduced a second equation:

$$h_{\mathrm{t},i} = c_p T_i \left(1 + \frac{\gamma - 1}{2} M_i^2\right) = c_p T_3 \left(1 + \frac{\gamma - 1}{2} M_3^2\right) = h_{\mathrm{t},3}, \tag{5}$$

while c_p and γ are the heat capacity at constant pressure, and heat capacity ratio, respectively. The third equation was the momentum equation, which originally was a vector equation:

$$\vec{F}_i = \int (\dot{m}_i \vec{v}_i + p_i \vec{n}_i)\, \mathrm{d}A_i = \int (\dot{m}_3 \vec{v}_3 + p_3 \vec{n}_3)\, \mathrm{d}A_3 = \vec{F}_3 \tag{6}$$

Because of the axisymmetric control volume, the momentum fluxes in the y- and z-direction canceled out each other, and equation (6) was transferred into a scalar equation:

$$F_{x,i} = \dot{m}_i v_i \cos(\alpha_i) + p_i A_i \sin(\theta_i) = \dot{m}_3 v_3 + p_3 A_3 = F_{x,3} \tag{7}$$

Therefore with equations (4), (5) and (7), as well as the equation of state and the expression for the Mach number, we were able to solve for the five unknowns: M_3, v_3, p_3, ρ_3 and T_3, which represent one-dimensional, and therefore so called stream thrust averaged variables. It is noted, that solving the three equations for the velocity led to a quadratic equation which essentially led to two results. Those two results are sometimes referred to as a subsonic and supersonic velocity, while in the present case the supersonic one was used. For a more detailed discussion about the stream thrust analysis in general, please refer to the cited literature[29–31].

Because a Busemann intake does not have an internal portion, the internal contraction ratio is usually equal to the overall contraction ratio.

$$CR_{\mathrm{o}} = \frac{A_\infty}{A_{\mathrm{cc}}}. \tag{8}$$

However, to quantify the influence of the rear side truncation, we defined the internal contraction ratio as

$$CR_{\mathrm{i}} = \frac{A_{\mathrm{cl}}}{A_{\mathrm{cc}}}, \tag{9}$$

The cross sectional areas are displayed in figure 1. With increasing rear side truncation, the intake exit area increased, and therefore the internal contraction ratios decreased. We investigated internal contraction ratios, ranging from $1.6 - 2.6$, in steps of 0.2, while the reference configuration, which will be described in the following section, had an internal contraction ratio of 2.9.

C. Reference Configuration

The reference configuration of the Busemann flow field followed the requirements of the German Research Training Group 1095[3]: The design point of the SCRamjet was at a Mach number of $M_\infty = 8$ and at an altitude of $h = 30\,\mathrm{km}$, with $226\,\mathrm{K}$ and $1170\,\mathrm{Pa}$ as the free stream temperature and pressure, respectively. For robust supersonic combustion we assumed that a static pressure in the combustion chamber of at least $50,000\,\mathrm{Pa}$ is required[1,32] and therefore a static pressure ratio of approximately $\Pi_{\mathrm{st}} \approx 43$ was taken as the design pressure ratio of the Busemann intakes. The exit area of the axisymmetric Busemann intake was set equal to the cross sectional area of the combustion chamber of the SCRamjet model, also designed in the Research Training Group 1095[7], and measured $A_{\mathrm{cc}} \approx 2700\,\mathrm{mm}^2$. Therefore the reference intake height of inviscid Busemann geometries was $h_{\mathrm{cc}} = 0.0294\,\mathrm{m}$. Please note, that the Euler simulations are independent of the intake size, and therefore the intake dimensions were given as fractions of the combustion chamber height, h_{cc}.

Consequently for the Euler simulations the following variables were needed as the design parameters: The free stream Mach number, M_∞, the static pressure ratio, Π_{st}, the truncation angle, δ, and the amount of rear side truncation, described by the internal contraction ratio, CR_{i}. Furthermore, for Reynolds-averaged Navier-Stokes (RANS) simulations, the wall temperature T_{w}, and the isolator height, h_{cc}, needed to be defined.

D. Numerical Modeling

The Reynolds-averaged Navier-Stokes (RANS) and Euler Simulations were performed with the DLR finite volume solver TAU[33]. The basic flow field and its boundary conditions were modeled according to figure 8. The

Centaur®(10.0.2) software package was used for the unstructured grid generation and the final grid size consisted of approximately $100,000$ grid points.

The grids that were used in the RANS simulations were structured at the viscous wall boundary with at least 30 prismatic layers, while $y+ < 1$ was ensured. Furthermore, the Wilcox $k-\omega$ SST turbulence model was used[34], and the wall was assumed to be isothermal. The boundary layer was assumed to be turbulent from the beginning.

For inhomogeneous flow, mass averaged and stream thrust averaged values were calculated for the CFD data with a self written Matlab ®(2012) routine.

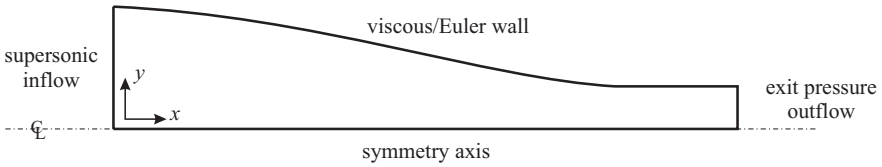

Figure 8. Numerical domain and boundary conditions for axisymmetric simulations of the Busemann flowfield.

III. Results

In this section we present and discuss the results for the different Busemann configurations, obtained with numerical simulations. The following two subsections give direct results to the two subsections in the Methods and Materials part (II., A. and B.). It is noted, that the results in subsection A. focus on the influence of additional contraction by the boundary layer, and therefore viscous simulations were performed. To investigate the effect of truncation, viscosity was neglected and therefore the results in subsection B. are extracted from Euler simulations.

A. Viscous Effects and Capability of Viscous Correction

In figure 9, wall pressure distributions for two different axisymmetric Busemann intakes, designed for the reference configuration described in section II., C. are plotted versus the axial distance, x. Results of the uncorrected contour (woVC) and for a geometry, that was corrected with a wall temperature of $T_{\mathrm{w}} = 900\,\mathrm{K}$, are displayed (wVC). Furthermore for this corrected geometry, the wall temperature was varied from $300\,\mathrm{K}$ to $1400\,\mathrm{K}$. In addition to the numerical results, the wall pressure distribution, predicted by the Busemann flow field is displayed. Finally, both geometries are displayed, and the increase in diameter due to the viscous correction is highlighted by the change in overall contraction ratio, and intake height at the combustion chamber interface, respectively.

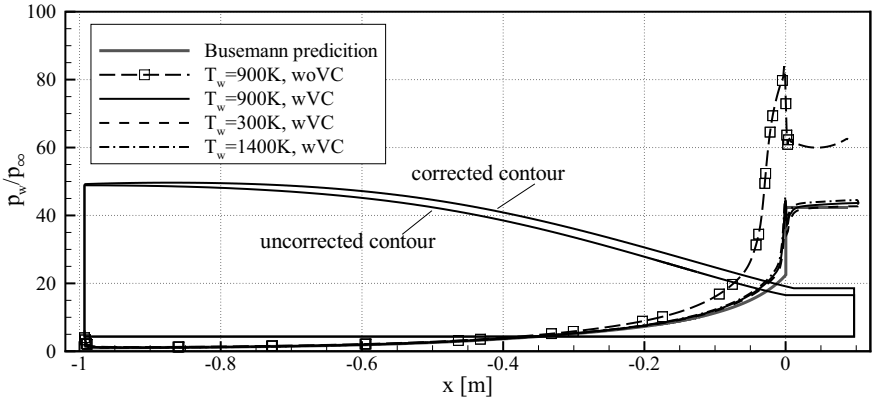

	A_∞/A_{cc}	$h_{\mathrm{cc}}[\mathrm{m}]$
woVC	13.5	0.0294
wVC	9.81	0.0342

Figure 9. Normalized wall pressure along x-coordinate for different configurations along with corrected and uncorrected Busemann contour; during viscous correction a constant wall temperature of 900 K was applied.

The wall pressure of the uncorrected contour exceeded the prediction by the Busemann flow field. The static pressure ratio at the intake exit lied at around 60, which is 40% higher than the design value. In contrast, the wall pressure of the corrected Busemann contour matched the pressure distribution of the Busemann prediction better. The static pressure ratio at the intake exit was very close to the design value of 43, and therefore the chosen integral method was suited well for predicting the additional contraction by the boundary layer. Furthermore for the same corrected geometry, the influence of wall temperature was investigated. Generally, with increasing wall temperature, the pressure level shifted to higher values. However this effect was weak, and therefore we suppose, that once a viscous correction was applied, it was valid for a broader temperature range ($\pm 500\,\mathrm{K}$). To ensure that the static pressure ratio from the

numerical simulations is at any case higher than the design pressure ratio, during the viscous correction we recommend to use a wall temperature at the lower range of wall temperatures expected.

1. Mach number variation

To verify the viscous correction at different free stream Mach numbers, we designed intakes, all for a static pressure ratio and an inviscid isolator height of $\Pi_{\mathrm{st}} = 43$ and $h_{\mathrm{cc,inv}} = 0.0294$ m, respectively, but varied the free stream Mach number, ranging from $M = 7$ to $M = 9$. We performed RANS simulations for the corrected geometries and results are plotted as normalized wall pressures, along with the Busemann predictions in figure 10.

For the investigated Mach number range, the viscous correction was able to properly account for viscous effects within the intake. Furthermore, the intake length increased with increasing free stream Mach number. The contraction ratio generally decreased with increasing free stream Mach number, however this effect was minor.

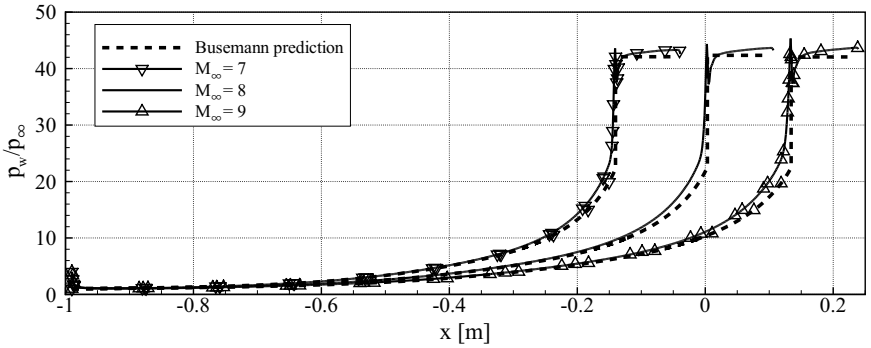

M_∞	A_∞/A_{cc}	h_{cc}[m]
7.0	9.86	0.0336
8.0	9.81	0.0342
9.0	9.58	0.0349

Figure 10. Normalized wall pressure along x-coordinate for different geometries; all intakes were designed for the specific free stream Mach number and for $\Pi_{\mathrm{st}} = 43$; viscous correction and numerical simulations were performed for $T_{\mathrm{w}} = 900$ K.

2. Size variation

To extend the validity of the viscous correction to different isolator heights, and therefore different intake sizes, we varied the inviscid isolator height and left the other reference configurations constant. In figure 11, results for geometries with half and double the reference inviscid isolator height are displayed and marked by $0.5h_{\mathrm{cc,inv}}$ and $2.0h_{\mathrm{cc,inv}}$, respectively. The viscous correction was again applied for a constant wall temperature of $T_{\mathrm{w}} = 900$K and the RANS simulations were performed for the same wall condition. Please note that the x-coordinate was normalized with the respective inviscid isolator height, to better compare the different results.

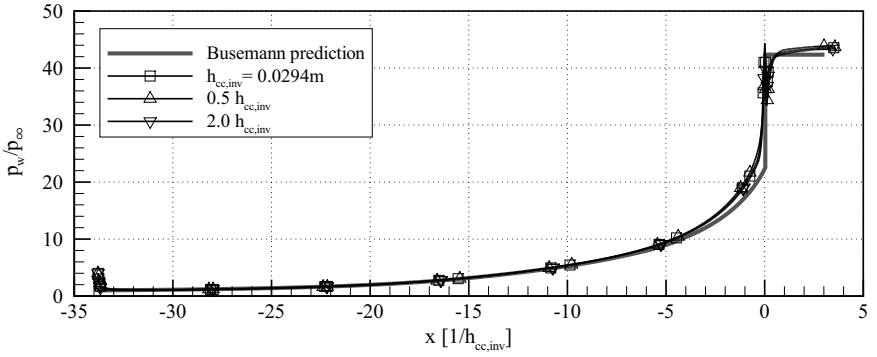

	A_∞/A_{cc}	h_{cc}[m]
1.0	9.81	0.0342
0.5	9.52	0.0174
2.0	10.06	0.0676

Figure 11. Normalized wall pressure along normalized x-coordinate for different isolator heights; all results are plotted for $T_{\mathrm{w}} = 900$ K, and with viscous correction at same wall temperature.

The wall pressure plots all fell onto the prescribed pressure level of 43. Therefore, the viscous correction was capable of considering different sizes and therefore different Reynolds numbers. Furthermore, the contraction ratio also increased with increasing intake size.

Finally we note, that in all cases investigated, the numerically calculated static pressure ratio was within 10% of the design value. Furthermore we conclude, that a viscous correction was necessary, if the driving design parameter is considered to be the static pressure ratio.

B. Truncation Effects

1. Leading Edge Truncation

In the present section the influence of the leading edge truncation on the intake flow field was investigated. In some cases, to assure a clear imaging, only every other truncation angle ($0°, 2°, 4°, 6°$) was displayed, but it is highlighted, that the validity of the conclusions was developed for results ranging from $0° - 7°$.

Wall pressure distributions, along with the intake contours are plotted for the truncated Busemann case in figure 12. With increasing truncation angle, the intake length and overall contraction ratio reduced. Furthermore, the wall pressure plots deviated stronger from the design pressure ratio of 43, which is also represented by the mean values in figure 13 a). Finally, due to the larger shock losses at higher deflection angles, the total pressure recoveries dropped (figure 13 d)).

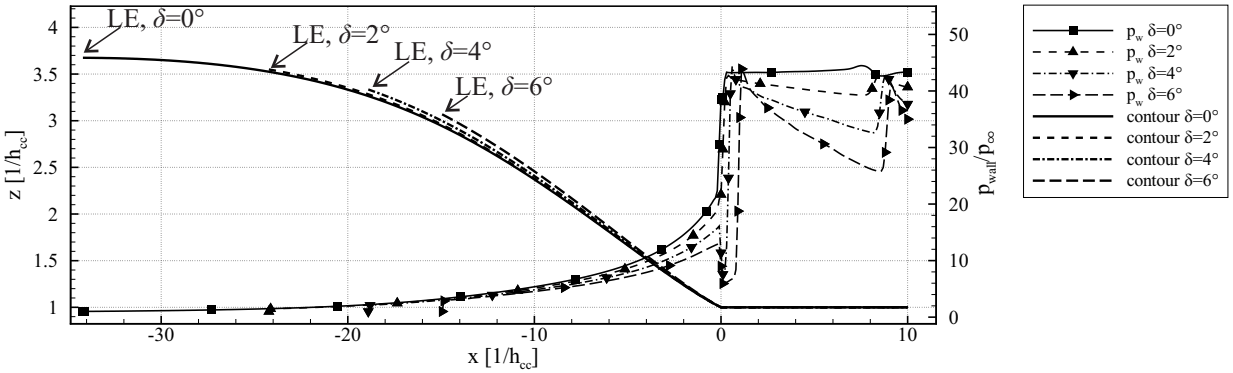

Figure 12. Busemann contours along with wall pressure distributions, plotted versus x-axis for different leading edge truncation angles; overall contraction ratio was not stretched.

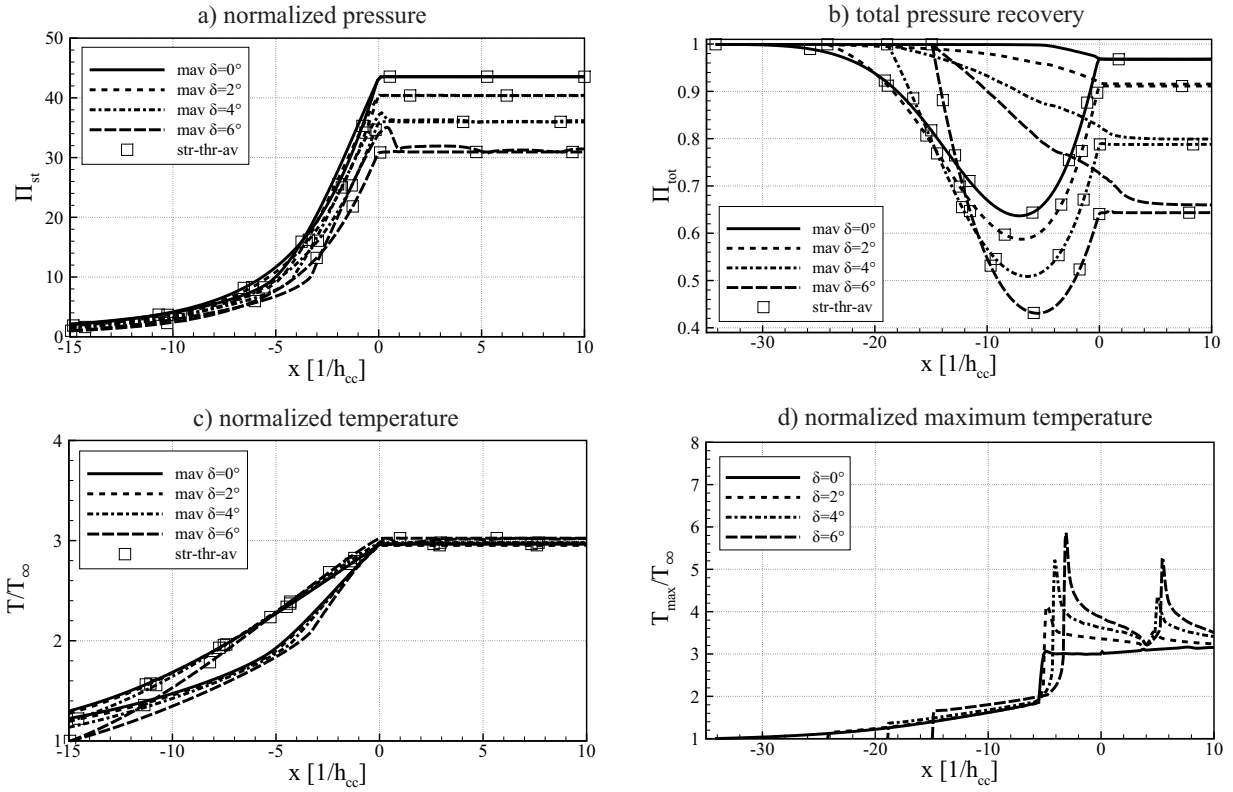

Figure 13. Influence of leading edge truncation on different variables; when applicable, mass averaged (mav) and stream thrust averaged (str-thr-av) values are shown; overall contraction ratio was not stretched.

On the other hand, the temperature levels in figure 13 c) remained approximately constant, and fell within 5% of the values predicted analytically (table 1). Furthermore, the maximum temperatures within the isolator increased with increasing truncation, which is a sign for non uniform flow.

Table 1. Design parameters for leading edge truncated Busemann intakes; all intakes designed for $M_\infty = 8$ and $\Pi_{st} = 43$.

$\delta[^\circ]$	0	1	2	3	4	5	6	7
Θ_{st}	2.95	2.95	2.96	2.97	2.99	3.02	3.06	3.11
$L[1/h_{cc}]$	34.2	28.2	24.2	21.3	18.9	16.9	14.9	13.1
CR_o	13.5	13.1	12.6	11.9	11.1	10.3	9.4	8.5
CR_i	2.90	2.90	2.92	2.94	2.96	2.99	3.03	3.08

Therefore we conclude, that with the leading edge truncated and the Busemann geometry not further stretched, the pressure levels from the CFD were lower than the predicted pressure levels, but the temperature levels were met correctly. In the further context we present our approach to maintain a constant pressure level: Since pressure levels were initially too low, we stretched the intake contraction ratio to higher levels, and took the contraction ratio of the 0° truncation case as a constant contraction ratio. Doing this resulted in pressure levels that were generally too high, but the absolute deviation from the design pressure level, for the two cases was approximately constant. Therefore we applied the half-stretching approach, which was explained in section II., and could keep the pressure level within 5% of the design value. Results are plotted in figure 14 for the different configurations.

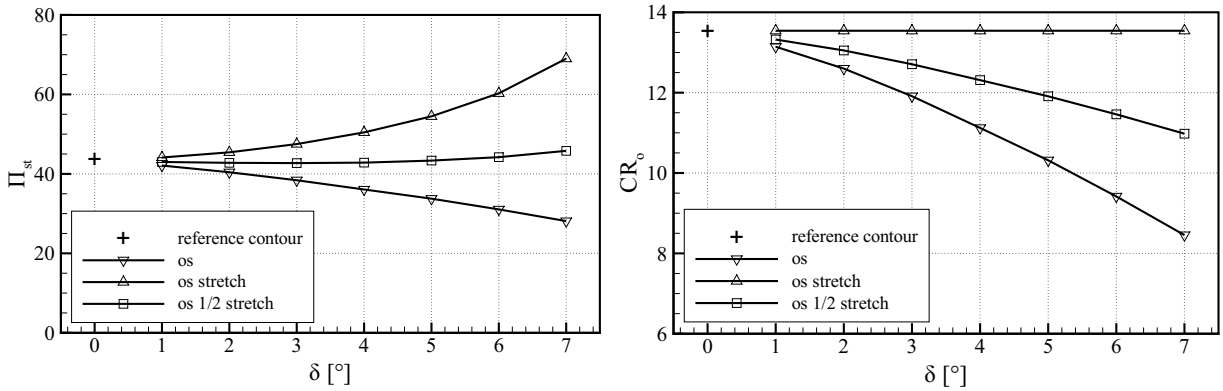

Figure 14. Stream thrust averaged static pressure ratios (left) and overall contraction ratios (right) plotted versus truncation angle; each symbol represents the results from one numerical simulation; data extracted at outlet.

Plots analogous to figure 12 and 13, for the half-stretching approach can be found in appendix B. To sum up, we highlight, that the design temperature levels were met correctly for the non stretched case, while in this case the pressure levels were generally too low. If the desired design parameter is the pressure level, the half stretching approach is recommended.

2. Rear Side Truncation

In the present section, the influence of rear side truncation on the intake flow was investigated. In some cases, to assure a clear imaging, only every other truncation case was displayed, but it is highlighted, that the validity of the conclusions was developed for the range described in section II. ($CR_i = 2.9 - 1.6$).

In figure 15, the intake contours along with the normalized wall pressure distributions are plotted for increasing rear side truncation. When truncating the intake at the rear side, the intake length was reduced. However the amount of reduction was smaller than in the leading edge truncation case. Furthermore with increasing rear side truncation, the wall pressure fluctuations around the design pressure level increased, which is a sign for a stronger non uniformity.

Table 2. Design parameters for Busemann intakes truncated at their rear side; all intakes designed for $M_\infty = 8$, $\delta = 0^\circ$ and $\Pi_{st} = 43$; intake with $CR_i = 2.9$ is non truncated geometry.

CR_i	(2.9)	2.6	2.4	2.2	2.0	1.8	1.6
Θ_{st}	2.95	3.01	3.06	3.12	3.18	3.25	3.32
$L[1/h_{cc}]$	34.2	32.7	31.8	31.0	30.1	29.3	28.4
CR_o	13.5	13.2	12.9	12.7	12.4	12.1	11.8

Because the wall pressure plots did not represent the mean flow characteristics, mass averaged as well as stream thrust averaged values are plotted in figure 16. The stream thrust averaged static pressure ratios (figure 16 – a)) matched the design pressure ratio of $\Pi_{st} = 43$ very accurately. With increasing rear side truncation, there was an increase in overshoot in mass averaged static pressure, which damped out further down the isolator. Total pressure

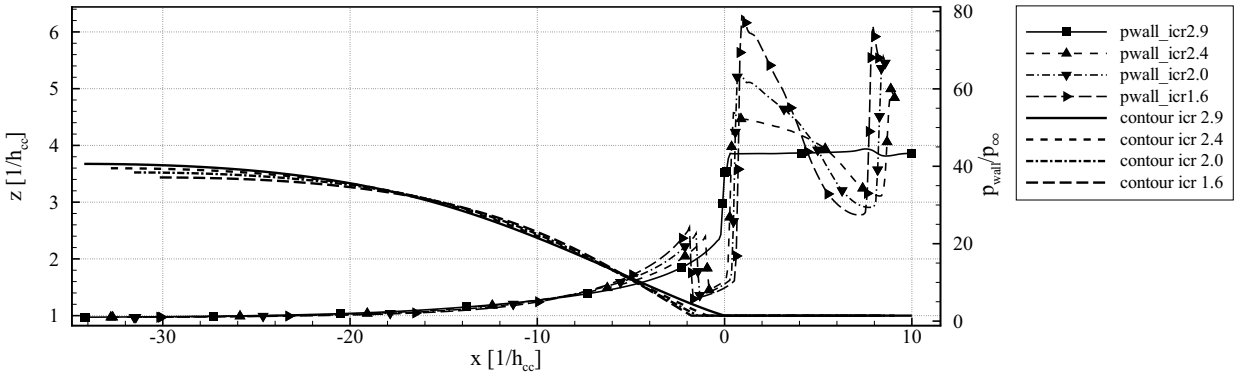

Figure 15. Busemann contours along with wall pressure distributions, plotted versus x-axis for different amounts of rear side truncation.

recoveries generally dropped with increasing rear side truncation (figure 16 – b)), while again the mass averaged values approached the constant plateau of the stream thrust averaged levels.

For increasing rear side truncation, the average static temperature levels increased (figure 16 – c)), and very nicely matched the analytical values from table 2. Analogously, the mass averaged profiles fluctuated stronger with increasing rear side truncation and damped out further downstream. Finally in (figure 16 – d)) the maximum static temperatures are plotted, and similarly to case c), the temperature level generally increased with increasing rear side truncation.

We conclude, that the stream thrust analysis was a valid tool to predict the change in flow properties, caused by the rear side truncation. The stream thrust averaged temperatures and pressures calculated from the CFD data were within 1% of the analtically predicted data. Furthermore, the non uniformity increased with increasing rear side truncation, which also decreased total pressure recovery. However the maximum temperature levels increased, which is beneficial for ignition.

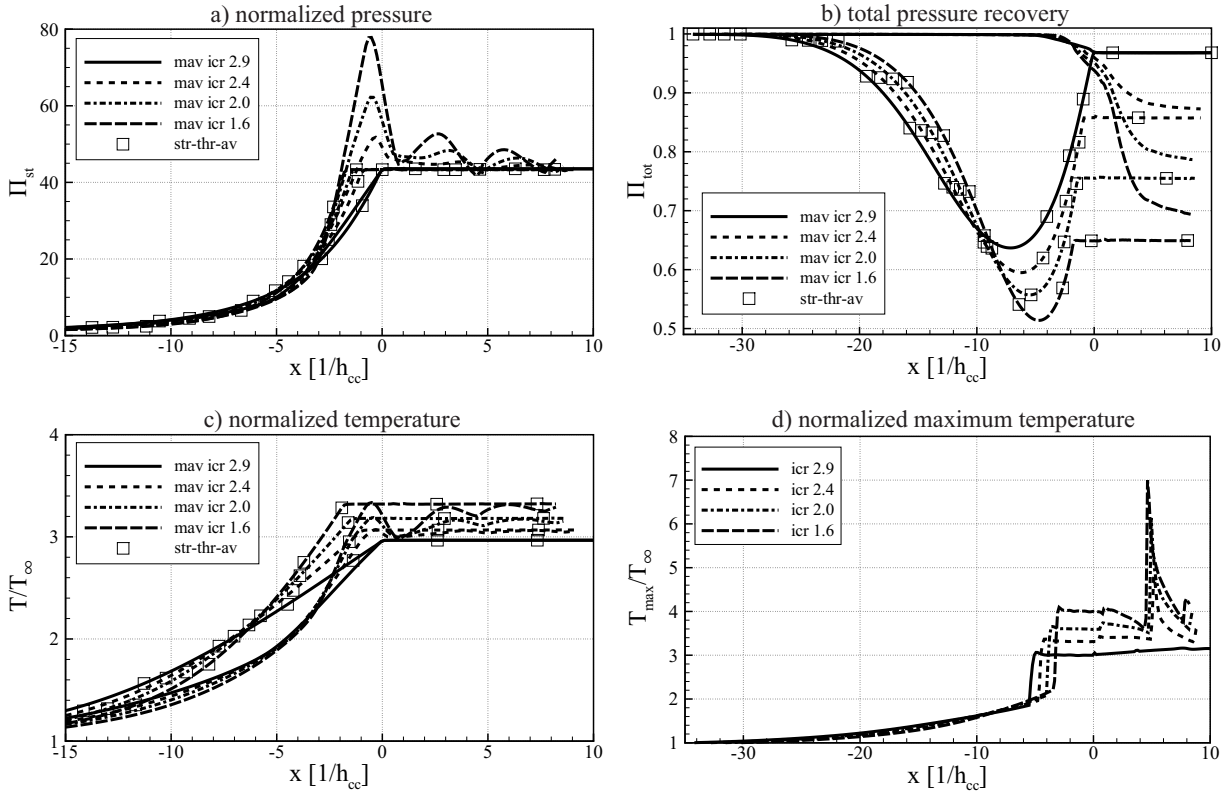

Figure 16. Influence of rear side truncation on various variables; when applicable, mass averaged (mav) and stream thrust averaged (str-thr-av) values are shown.

IV. Conclusion

In the present paper we focused on axisymmetric Busemann intakes. We identified viscous and truncation effects, while in the latter case we distinguished between intakes that were truncated at the leading edge and intakes that were truncated at the rear side. For the different effects we proposed different approaches to quantify the changes in the flow properties. Various configurations were investigated numerically with Euler or if applicable RANS simulations and results were compared to analytically predicted data.

Generally all effects influenced the classical Busemann flow field while the main findings were:

1. Widening the classical contour with the boundary layer displacement thickness, which we calculated with an integral method, kept the deviation between CFD and analytical prediction below 10%.

2. The range of validity of the viscous correction was extended to Mach numbers between 7 and 9 and to double and half the reference size.

3. Intake length could successfully be reduced by truncating the intake, while the leading edge truncation was more effective; both truncation approaches decreased total pressure recovery.

4. Non uniformity, with higher maximum temperatures could be generated with increasing truncation, while the rear side truncation was more effective; this could enhance mixing, as well as ignition.

5. The leading edge truncation was modeled with an oblique shock; with increasing truncation, the numerically calculated pressures were observed to be lower than the predictions; the temperatures were predicted properly.

6. To properly predict the pressure ratios in the leading edge truncation case, we proposed a half-stretching approach, where the intake contraction ratio was stretched to a larger value; this led to a proper prediction of the pressure levels, but the temperature levels increased.

7. The influence on the flow properties, caused by the rear side truncation were modeled with a stream thrust analysis; this approach was highly accurate, and the stream thrust averaged pressures and temperatures, extracted from CFD, were within 1% of the analytical prediction.

Appendix A – Transition Modeling in Integral Method

In figure 17, the data set of Berkowitz is plotted as the probability density function (left) and the cumulative density function (right), which is the integral of the former.

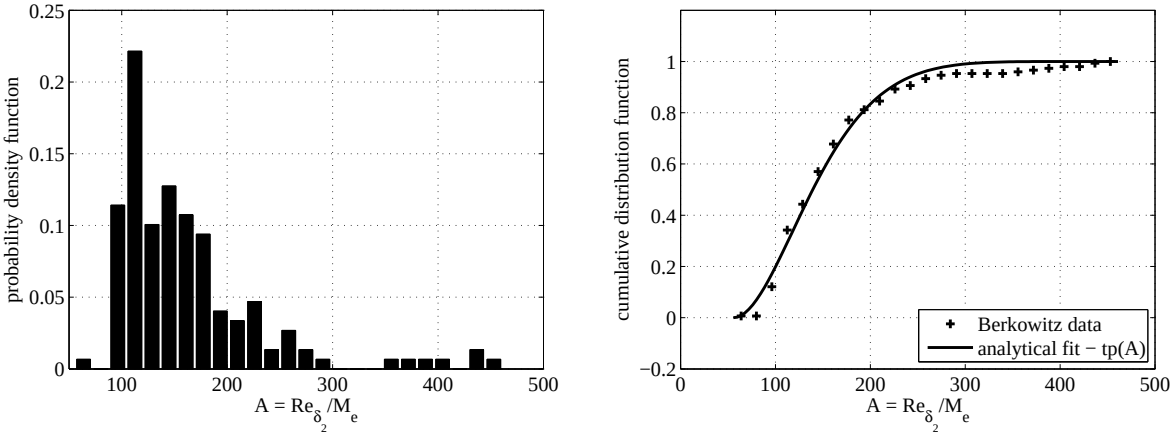

Figure 17. Data set of Berkowitz [27], plotted as probability density function and cumulative density function, along with analytical function, $tp(A)$.

We approximated the gradual transition from laminar to turbulent with an analytical fit, $tp(A)$, which is given in the following equations:

$$tp(A) = \frac{1}{2}\left(\sin\left(\frac{f(A) - A_{\min}}{A_{\max} - A_{\min}}\pi - \frac{\pi}{2}\right) + 1\right) \tag{10}$$

$$f(A) = -\frac{|A - A_{\max}|^n}{(A_{\max} - A_{\min})^n} + A_{\max} \tag{11}$$

$$A = \frac{Re_{\delta_2}}{M_e}, A_{\min} = 56, A_{\max} = 461, n = 3 \tag{12}$$

Appendix B – Results for Half-Stretching Approach

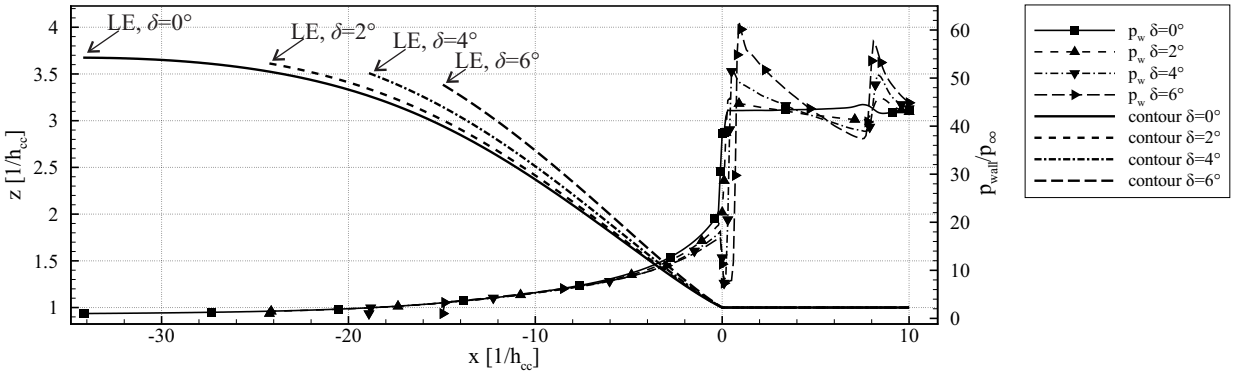

Figure 18. Busemann contours along with wall pressure distributions, plotted versus x-axis for different leading edge truncation angles; half-stretching was applied.

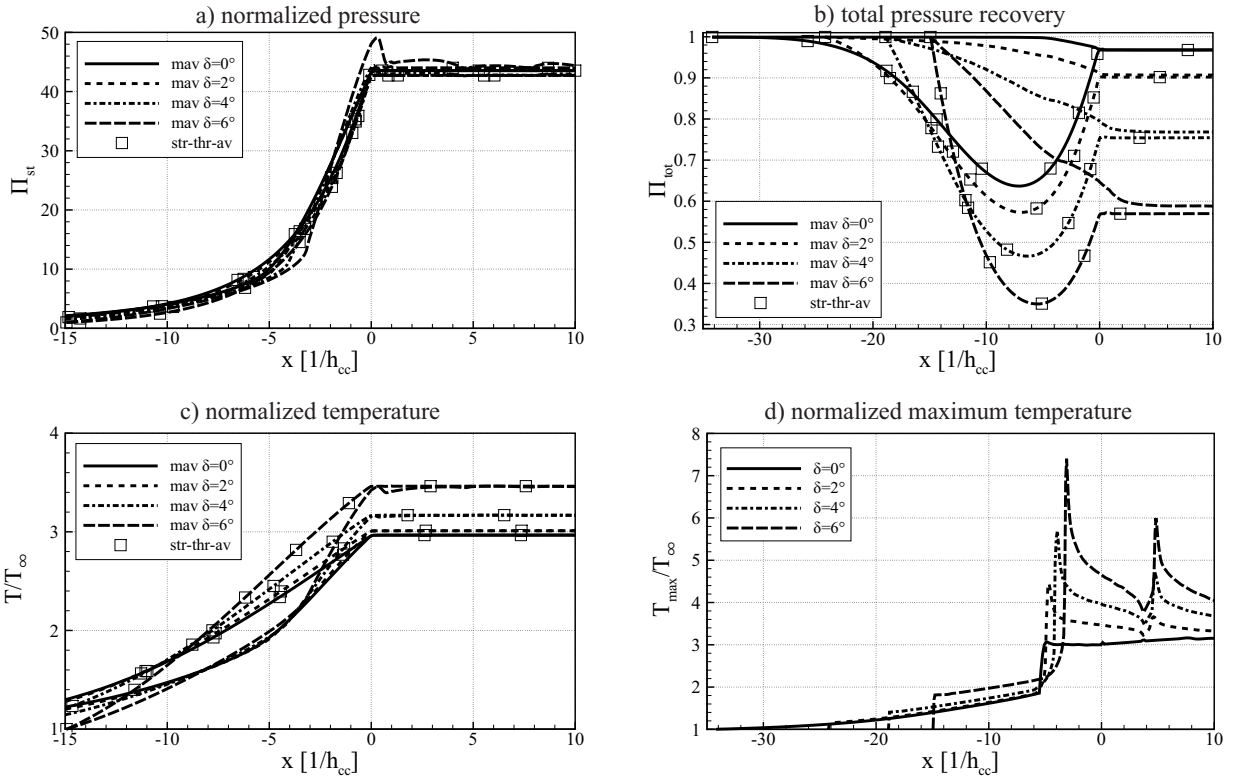

Figure 19. Influence of leading edge truncation on various variables; when applicable, mass averaged (mav) and stream thrust averaged (str-thr-av) values are shown; half-stretching was applied.

Acknowledgments

The present work was funded within the Research Training Group 1095/2. We would like to thank the German Research Foundation (DFG) for the support during that period.

References

[1]Heiser, W. H. and Pratt, D. T., *Hypersonic Airbreathing Propulsion*, AIAA Education Series, 1994.

[2]Wie, D. M. V., "Scramjet Inlets," *Scramjet Propulsion*, edited by E. T. Curran and S. Murthy, Progress in Astronautics and Aeronautics, 2000, pp. 447–511.

[3]Weigand, B. and Gaisbauer, U., "An Overview on the Structure and Work of the DFG Research Training Group GRK 1095: "Aero-Thermodynamic Design of a Scramjet Propulsion System"," *16th AIAA International Space Planes and Hypersonic Systems and Technologies Conference*, 2009.

[4]Häberle, J. and Gülhan, A., "Experimental Investigation of a Two-Dimensional and a Three-Dimensional Scramjet Inlet at Mach 7," *Journal of Propulsion and Power*, Vol. 24, No. 5, Sept. 2008, pp. 1023–1034.

[5]Hohn, O. M. and Gülhan, A., "Experimental Investigation on the Influence of Sidewall Compression on the Flowfield of a Scramjet Inlet at Mach 7," *International Space Planes and Hypersonic Systems and Technologies Conference*, No. April, 2011, pp. 1–17.

[6]Hohn, O. M. and Gülhan, A., "Analysis of a Three-Dimensional , High Pressure Ratio Scramjet Inlet with Variable Internal Contraction," *18th AIAA/3AF International Space Planes and Hypersonics Systems and Technologies Conference*, No. September, 2012.

[7]Riehmer, J. C. and Gülhan, A., "Simulation of combustion by cold air injection in a generic scramjet model in the H2K blow down facility," *5th European Conference for Aeronautics and Space Sciences*, 2013.

[8]Flock, A. K. and Gülhan, A., "Experimental Investigation of the Starting Behavior of a three-dimensional SCRamjet Intake with a Movable Cowl and Exchangeable Cowl Geometry at Different Mach Numbers," *19th AIAA International Space Planes and Hypersonic Systems and Technologies Conference*, June 2014, pp. 1–12.

[9]Hermann, R., *Supersonic Inlet Diffusers and Introduction to Internal Aerodynamics*, Minneapolis-Honeywell Regulator Company, Minneapolis, Minnesota, 1956.

[10]Oswatitsch, K., "Pressure Recovery for Missiles with Reaction Propulsion at High Supersonic Speeds," *National Advisory Committee for Aeronautics*, 1944.

[11]Busemann, A., "Die achsensymmetrische kegel-Überschallströmung," *Luftfahrforschung*, Vol. 19, 1942, pp. 137–144.

[12]Yu, Y.-N., "A Summary of Design Techniques for Axisymmetric Hypersonic Wind Tunnels," Tech. Rep. November 1958, 1958.

[13]Cronvich, L. L., "A Numerical-graphical method of characteristics for axially symmetric isentropic flow," *Journal of the Aeronautical Sciences*, Vol. 15, No. 3, 1948, pp. 155–162.

[14]Anderson, J. D. J., *Modern Compressible Flow*, McGraw Hill, 1990.

[15]Smart, M. K., "Design of Three-Dimensional Hypersonic Inlets with Rectangular-to-Elliptical Shape Transition," *Journal of Propulsion and Power*, Vol. 15, No. 3, May 1999, pp. 408–416.

[16]Wie, D. M. V. and Mölder, S., "Applications of Busemann Inlet Designs for Flight at Hypersonic Speeds," *AIAA Journal*, 1992.

[17]Billig, F. S. and Kothari, A. P., "Streamline Tracing: Technique for Designing Hypersonic Vehicles," *Journal of Propulsion and Power*, Vol. 16, No. 3, 2000, pp. 465–471.

[18]Mölder, S. and Szpiro, E. J., "Busemann Inlet for Hypersonic Speeds," *AIAA Journal*, Vol. 3, No. 8, 1966, pp. 1303–1304.

[19]Arens, T., Hettlich, F., Karpfinger, C., Kockelkorn, U., Lichtenegger, K., and Stachel, H., *Mathematik*, Spektrum Akademischer Verlag, Heidelberg, 2008.

[20]Walsh, P., Tahir, R. B., and Mölder, S., "Boundary-layer Correction for the Busemann Hypersonic Air Inlet," *Canadian Aeronautics and Space Journal*, Vol. 49, No. 1, 2003, pp. 11–17.

[21]Zhao, Z. and Song, W., "Effect of Truncation on the Performance of Busemann Inlet," *Modern Applied Science*, Vol. 3, No. 2, 2009, pp. 168–171.

[22]Veillard, X., Tahir, R., Timofeev, E., and Mölder, S., "Limiting Contractions for Starting Simple Ramp-Type Scramjet Intakes with Overboard Spillage," *Journal of Propulsion and Power*, Vol. 24, No. 5, 2008, pp. 1–8.

[23]Timofeev, E. V., Tahir, R. B., and Mölder, S., "On Recent Developments Related to Flow Starting in Hypersonic Air Intakes," *15th AIAA International Space Planes and Hypersonic Systems and Technologies Conference*, No. May, 2008, pp. 1–9.

[24]Jacobsen, L. S., Tam, C.-j., Behdadnia, R., and Billig, F. S., "Starting and Operation of a Streamline-Traced Busemann Inlet at Mach 4," *42nd AIAA/ASME/SAE/ASEE Joint Propulsion Conference & Exhibit*, No. July, 2006, pp. 1–19.

[25]Wie, D. M. V., Kwok, F. T., and Walsh, R. F., "Starting Characteristics of Supersonic Inlets," *AIAA meetings papers*, , No. July, 1996.

[26]Walz, A., *Strömungs- und Temperaturgrenzschichten*, Verlag G. Braun, Karlsruhe, 1966.

[27]Berkowitz, A., Kyriss, C., and Martellucci, A., "Boundary Layer Transition Flight Test Observations," *AIAA 15th Aerospace Sciences Meeting*, 1977.

[28]Hirschel, E. H., *Basics of Aerothermodynamics*, Springer, 2005.

[29]Curran, E. T., "The Use of Stream Thrust Concepts for the Approximate Evaluation of Hypersonic Ramjet Engine Performance," Tech. rep., 1973.

[30]Baurle, R. A. and Gaffney, R. L., "The Art of Extracting One-Dimensional Flow Properties from Multi-Dimensional Data Sets," *45th Aerospace Sciences Meeting and Exhibit*, 2007.

[31]Rolim, T. and Lu, F., "Design and Stream Thrust Analysis of a Scramjet Engine for Acceleration Mission from 2 to 3 km/s," *51st AIAA Aerospace Sciences Meeting*, No. January, 2013, pp. 1–16.

[32]Smart, M. K., "How Much Compression Should a Scramjet Inlet Do ?" *AIAA Journal*, Vol. 50, No. 3, 2012, pp. 610–619.

[33]DLR, "The DLR TAU code - http://tau.dlr.de," .

[34]Menter, F. R., Kuntz, M., and Langtry, R., "Ten Years of Industrial Experience with the SST Turbulence Model," *Heat and Mass Transfer*, Vol. 4, 2003.